Journal of Nuclear Materials 402 (2010) 30–37

Contents lists available at ScienceDirect

Journal of Nuclear Materials

journal homepage: www.elsevier.com/locate/jnucmat

Formation of Y_2O_3 nanoclusters in nano-structured ferritic alloys: Modeling of precipitation kinetics and yield strength

Céline Hin [a,b,*], Brian D. Wirth [a]

[a] Department of Nuclear Engineering, University of California, Berkeley, CA 94720-1730, USA
[b] Department of Materials Sciences and Engineering, Massachusetts Institute of Technology, Cambridge, MA 02139-4307, USA

ARTICLE INFO

Article history:
Received 17 May 2009
Accepted 21 April 2010

ABSTRACT

The solubility product of Y_2O_3 in ferrite and the diffusion coefficient of yttrium in ferrite have been obtained by fitting a model based on the classical nucleation–growth–coarsening theory of precipitation, as adapted to an anisothermal heat treatment, to experimental small angle neutron scattering results of Y_2O_3 precipitate size distributions in a mechanically alloyed and consolidated Fe–15 at.%Cr–0.13 at.%Y–0.18 at.%O ferritic alloy. This precipitation model is coupled to a dispersed barrier model of structural hardening to predict the yield strength of the alloys as a function of heat treatment. The resulting model and thermodynamic/kinetic properties are then applied to better understand how the precipitation kinetics impact the yield stress in various anisothermal heat treatments, as compared to an isothermal heat treatment. The modeling results clearly indicate that the anisothermal heat treatments can be tailored to establish a higher density and a smaller size distribution of Y_2O_3 precipitates, which also increase the yield stress.

1. Introduction

Advanced ferritic alloys containing a very high number density of embedded nanoscale Y–Ti–O precipitate clusters, which are an improved variant of conventional oxide dispersion strengthened (ODS) alloys, are attractive for future high temperature energy production technologies. These advanced ferritic alloys are known for improved creep resistance at high temperatures compared to other ODS alloys, and may provide a potent trap for the insoluble helium produced by transmutation reactions in future fusion energy production [1–5]. A key characteristic of these advanced, nanoscale ferritic alloys (NFAs) compared to more conventional ODS alloys, is the observation of Ti within the Y–Ti–O nanoscale precipitate clusters, which is believed responsible for the improved high temperature strength and stability of these alloys, as reviewed recently by Odette and co-workers [6]. These alloys are currently under development in the United States and Europe [7–16], as well as in Japan [17–22].

However many questions still exist as to how the formation, structure, and thermal stability of these Y–Ti–O nanoparticles affect the optimal processing method and their performance in extreme environments, in addition to asses their promise for radiation resistance in nuclear environments [6]. It is thus necessary to understand the kinetics of precipitation after both the mechanical alloying and the thermo-mechanical consolidation treatment, which involves in this study an anisothermal heat treatment induced by the consolidation by HIP. As a first stage in developing understanding of the nanocluster precipitation kinetics, we will describe here the use of classical nucleation–growth–coarsening theory to describe the precipitation kinetics of Y_2O_3 in ferritic alloys. These models can later be extended to the more complicated situation of the Y–Ti–O nanoclusters in NFA.

The classical nucleation–growth–coarsening theory based on the model of Langer and Schwartz [23] and modified by Kampmann and Wagner [24] provides an understanding of the kinetics of precipitation in super-saturated alloys. The precipitation kinetics of a metastable solid solution can be divided into three different stages: namely, nucleation (N), growth (G) and coarsening (C) of nuclei of the new stable phase. However, it is well known that these different NGC kinetic regimes usually overlap and have been integrated in unified models to study isothermal kinetics of homogeneous [25–27] and heterogeneous [28,29] precipitations, or non-isothermal kinetics of homogeneous precipitation [30–33]. Kinetics of homogeneous precipitation during welding has also been explored [34,35]. As well, some NGC models have also been coupled to models of structural hardening to predict the materials yield stress [27,28,31,34], as has also been done in the current study.

The key physical parameters of classical NGC theory are the interfacial free energies, the solubility product, and the diffusion coefficient. Since these parameters are very difficult to estimate directly from experiments in multi-component systems, especially those prone to impurity contamination, there is a lack of reliable

---

[*] Corresponding author at: Department of Materials Sciences and Engineering, Massachusetts Institute of Technology, Cambridge, MA 02139-4307, USA.
E-mail address: celine_hin@yahoo.fr (C. Hin).

0022-3115/$ - see front matter © 2010 Elsevier B.V. All rights reserved.
doi:10.1016/j.jnucmat.2010.04.020

experimental data on these quantities in the complex Fe–Cr–Y–Ti–O alloy system.

One goal of this study is to provide an estimate of these key parameters in ternary Fe–Y–O alloys by comparing model predictions to experimental measurements of Y_2O_3 precipitate evolution in an Fe–15 at.%Cr or Fe–15 at.%Cr–0.8 at.%W ferrite matrix [36]; and then to understand the effect of anisothermal heat treatment on the density and the size of these nanometer-sized precipitates. Starting from this microstructural evolution, the link will be made with the precipitation hardening. The results of this work provide the foundation for further study to investigate the kinetic precipitation pathway in quaternary Fe–Ti–Y–O alloys.

In the next section, the conditions used to obtain experimental data in the work of Alinger are first discussed [36]. Then, a numerical model based on the classical NGC theory and adapted to the case of anisothermal heat treatment will describe quantitatively the various relevant parameters of the precipitation process, such as the mean precipitate radius or the number density, which can be compared to the various situations explored experimentally by Alinger [36]. The NGC model has been coupled with a model for precipitation hardening, which considers the transition between precipitate shearing and Orowan looping for dislocation detachment, which is based on the work by several groups [27,30,37–39]. For an average precipitate radius smaller than a transition radius, the precipitates are assumed sheared by dislocations. Otherwise, the precipitates are by-passed by Orowan looping. In the case of nanostructured ODS alloys, the dislocation interaction and bypass mechanism is not the same. For small oxide particle sizes, precipitates are sheared. However, when precipitates grow and lose their coherency, a model for the effect of an attractive interaction between dislocation and oxides (considered as a hard sphere particle) on the process of dislocations by-passed by local climb was developed [40–42]. This model is explained in Section 3. Section 4 is devoted to discussing the effect of the heating rate in anisothermal heat treatments, and comparison of the precipitation kinetics between anisothermal and isothermal heat treatments, and this represents a significant extension of the current model compared to studies in the literature. The model will also be used to evaluate the role of different levels of Y and O supersaturations on the precipitation kinetics during anisothermal heat treatment. Finally, the influence of the different microstructures of precipitation on the micro-hardness obtained during different heat treatment history and alloy compositions will be analyzed.

2. Determination of the solubility product

2.1. Experimental study

Many experimental studies have investigated the formation of a high density, and apparently coherent, nm-sized Y–O–Ti precipitate clusters produced by mechanically alloying Fe–Cr–Ti powders with Y_2O_3 followed by hot consolidation [1–5,36,43]. The work of Alinger [36] included a study of Y_2O_3 precipitation in Fe–Cr alloys, without the inclusion of titanium, which can be used to obtain an approximation of both the solubility product of Y_2O_3 and the diffusion coefficient of yttrium in ferrite.

In Ref. [36], mechanical alloying was used to incorporate Y_2O_3 powders within a ferrite matrix formed from Fe–15 at.%Cr or Fe–15 at.%Cr–0.8 at.%W powders. The mechanical alloying process is highly non-equilibrium, with large levels of plastic deformation added to the powders. It is relatively well established that the mechanical alloying process involves significant work hardening and ultimate fracture of the powders that results in grain size reductions, increases the dislocation density and incorporates super-saturated levels of nearly insoluble elements. The mechanical alloying procedure of Alinger [36] utilized an approximately 8 h mixing in a SPEX 80000 attritor mill, during which the yttrium and oxygen are absorbed into highly super-saturated solution in the FeCr ferrite matrix [36]. Alinger et al. [6,36,44] then used hot isostatic pressing (HIP) to consolidate the powders with an isotropic pressure of 200 MPa, and various anisothermal heating profiles with temperature plateau's of 1125 and 1425 K and a hold-time of 3 h. The heating rate was generally 0.33 K/s, while the cool down rate was approximately 0.25 K/s [36]. Small angle neutron scattering (SANS) was used to determine the average Y_2O_3 precipitate size, number density and volume fraction [36].

To summarize the experimental data of Alinger [36], the SANS measurements for different alloys composition are provided in Table 1. Thus, anisothermal HIP treatment with a plateau at 1125 K produces many small precipitates, while the higher temperature anisothermal HIP treatment produces significantly fewer, but larger precipitates, in which it is tempting to conclude that the precipitation kinetics has already entered the coarsening stage. Furthermore, the amount of W in the alloys does not appear to influence the density and radius of precipitates. All these data will be compared to the model predictions.

2.2. Mathematical modeling

2.2.1. Model assumptions

The homogeneous anisothermal precipitation model developed is partly based on the work of Langer and Schwartz [23], as modified by Kampmann and Wagner (MLS) [24]. The three different NGC stages are treated simultaneously, assuming that precipitates with a radius smaller than the critical radius dissolve. At each time step, the nucleation and growth/dissolution equations are simultaneously treated, ensuring coarsening of the precipitates driven by the Gibbs–Thomson effect [45]. This algorithm allows precipitation at any time within the time–temperature history of any possible heat treatment (e.g. in our case, an anisothermal aging).

In order to keep the model at a reasonable level of simplicity and number of parameters, some significant simplifications have been made:

- the stoichiometric Y_2O_3 phase is the only precipitate phase and Cr is not involved in the Y_2O_3 precipitation kinetics;
- the precipitates are spherical and do not induce a strain field in the matrix;
- there is no interaction between precipitates;
- the precipitate/matrix interfacial energy depends on neither temperature nor the precipitate size. In Ref. [46], the authors note that this assumption becomes valid only for precipitate sizes larger than 20 atoms;
- the interfacial condition is based on the assumption of local equilibrium, namely that the concentration at the precipitate/matrix interface is given by the phase diagram (e.g. the solubility product) corrected by the interface curvature [45];
- the precipitate growth is limited by monomer diffusivity. The low diffusivity of yttrium is found to be limiting for all stages of precipitation in the Fe–Y–O alloy system. Whereas, the oxygen atoms are at thermodynamic equilibrium to uniquely ensure the stoichiometry of the Y_2O_3 precipitate; and that
- the concentration profile around the precipitates is stationary.

2.2.2. Thermodynamics of the model

Using an ideal solution model, the activities of the elements in solid solution can be approximately proportional to their atomic fractions. Assuming that the oxidation reaction can be written as $2Y + 3O \rightarrow Y_2O_3$, the driving force for precipitation at any given

Table 1
SANS results for different ODS alloy compositions and different anisothermal heat treatment.

Alloy	Alloy elements (at.%)					Milling technique	Process	Consolidation temperature (K)	Precipitate radius (nm)	Precipitate density (m^{-3})
	Cr	Ti	W	Y	O					
U14Y	15	–	–	0.13	0.18	SPEX	HIP	1125	1.37	0.94×10^{24}
U14Y	15	–	–	0.13	0.18	SPEX	HIP	1425	4.88	0.13×10^{23}
U14YW	15	–	0.8	0.13	0.18	SPEX	HIP	1125	1.43	0.11×10^{25}
U14YW	15	–	0.8	0.13	0.18	SPEX	HIP	1425	5.39	0.79×10^{22}
014Y	15	–	–	0.13	0.18	Attritor	HIP	1125	1.37	0.69×10^{24}
014Y	15	–	–	0.13	0.18	Attritor	HIP	1275	1.49	0.44×10^{24}

time and temperature within the anisothermal heat treatment can then be derived as:

$$\Delta g = -\frac{kT}{V_{Y_2O_3}} \ln\left(\frac{X_O^3 \times X_{Y^2}}{K_{Y_2O_3}}\right) = -\frac{kT}{V_{Y_2O_3}} \ln S_{Y_2O_3}, \tag{1}$$

where $V_{Y_2O_3}$ is the atomic volume, X_O and X_Y are the atomic fractions of oxygen and yttrium in the bulk, respectively, $K_{Y_2O_3}$ is the solubility product of Y_2O_3 in ferrite, and $S_{Y_2O_3}$ is the supersaturation of the solid solution with respect to Y_2O_3 precipitation. The solubility product corresponding to pure homogeneous nucleation is unknown. Thus this parameter has been considered adjustable for the nucleation of Y_2O_3 precipitates in ferrite.

From the thermodynamic driving force, the critical radius R^* of a nuclei at a given matrix concentration of yttrium and oxygen can be derived as:

$$R^* = -\frac{2\gamma}{\Delta g} = \frac{R_0}{\ln S_{Y_2O_3}} \quad \text{with} \quad R_0 = -\frac{2\gamma V_{Y_2O_3}}{kT}, \tag{2}$$

where γ is the interface free energy between the Y_2O_3 precipitates and the matrix.

The nucleation barrier can then be described as:

$$\Delta G^* = \frac{16}{3}\pi\frac{\gamma^3}{\Delta g^2} = \frac{\Delta G_0}{(\ln S_{Y_2O_3})^2} \quad \text{with} \quad \Delta G_0 = \frac{4}{3}\pi R_0^2 \gamma. \tag{3}$$

Here ΔG^* is the energy barrier that must be crossed for a sub-critical nucleus to grow.

2.2.3. Nucleation, growth and coarsening

2.2.3.1. Nucleation. The nucleation rate is taken as that previously derived by Christian [47]:

$$\frac{dN_n}{dt} = N_0 Z \beta^* \exp\left(-\frac{\Delta G^*}{kT}\right)\left[1 - \exp\left(-\frac{t}{\tau}\right)\right]. \tag{4}$$

Here, N_n is the precipitate density, N_0 is the number of available nucleation sites per unit volume ($=1/V_{Fe}$), Z is the Zeldovitch factor that describes size fluctuations of precipitates around R^* and β^* is the condensation rate for clusters of a critical size. Assuming that the limiting step of the adsorption is the last atomic jump of the solute atom from the matrix toward the surface of the precipitate of critical size, the condensation rate is given by:

$$\beta^* = \frac{4\pi R^{*2} D X}{a_{Fe}^4}. \tag{5}$$

Assuming that yttrium is the slowest diffusing species leads to the use of $X = X_Y$ and $D = D_Y$. Finally, the incubation time, τ, can be written as:

$$\tau = \frac{1}{2\beta^* Z}. \tag{6}$$

2.2.3.2. Growth and coarsening. In the later stages of precipitation, the nucleation rate in the solid solution progressively decreases as the level of super saturation decreases, and the alloy experiences a combination of growth and coarsening. Correspondingly, the evolution of the precipitate radius is given by:

$$\frac{dR}{dt} = \frac{D}{R}\frac{\frac{X}{V_{Fe}} - \frac{X^i}{V_{Fe}}}{\frac{X^{pp}}{V_{Y_2O_3}} - \frac{X^i}{V_{Fe}}} = \frac{D}{R}\frac{X - X^i}{\frac{X^{pp}}{V_{Y_2O_3}} - X^i}. \tag{7}$$

To evaluate X^i (the atomic fraction at the precipitate/matrix interface), the local equilibrium assumption is used and stipules that $X_O^{i3} \times X_Y^{i2}$ at the precipitate/matrix interface is equal to the solubility product $K_{Y_2O_3}$. As we take into account the curvature effect, the solubility product becomes:

$$K_{Y_2O_3}(R) = K_{Y_2O_3} \exp\left(\frac{R_0}{R}\right). \tag{8}$$

This NGC model reduces to a set of three equations with three unknowns (dR/dt), X_O^i and X_Y^i, which can be solved numerically. These equations are:

$$\frac{dR}{dt} = \frac{D_Y}{R}\frac{X_{Y - X_{Y^i}}}{X_{Y^{pp}\frac{V_{Fe}}{V_{Y_2O_3}} - X_{Y^i}}} = \frac{D_O}{R}\frac{X_O - X_O^i}{X_O^{pp}\frac{V_{Fe}}{V_{Y_2O_3}} - X_O^i} X_Y^{i2} \times X_O^{i3}$$
$$= K_S \exp\left(\frac{R_0}{R}\right). \tag{9}$$

To treat the coarsening stage, it is assumed that coarsening is completely included in the growth stage. Because the Gibbs–Thomson effect is included in Eq. (9), the dissolution of the smaller precipitates is assured. Furthermore, precipitates with a radius smaller than the critical radius dissolve. Finally, since the concentration of solute atoms in the bulk is recalculated at each time step by performing a global solute balance that subtracts the quantity of solute atoms contained in the Y_2O_3 stoichiometric precipitates from the initial solute concentration, the total concentration in solute atoms is conserved.

2.2.4. Numerical solution of the model

The numerical method used to solve the NGC equations is a "size class model". It allows us to solve a variable number of independent differential equations, giving the nucleation rates and the growth of each precipitate class at each time step.

Thus at each time t, $N_{classes}(t)$ classes of particles of volume density $N_i(t)$ are associated with particles of radius $R_i(t)$ with $i \in [1, N_{classes}(t)]$. A set of differential equations is then solved using the finite difference method with an elementary time step Δt: (i) the nucleation equation provides the number ΔN of sub-critical nuclei per unit volume during Δt, and (ii) $N_{classes}(t)$ of growth equations provide the radius variation ΔR_i of each class i of particles during Δt. After each step, the temperature can be adjusted to account for anisothermal heat treatments. The temperature is increased by 0.33 K/s, as was followed in the HIPing procedure of Alinger [36]. A very small elementary time step (e.g. $\Delta t = 0.05$ s) is chosen to ensure a quasi-continuous description.

A new class of precipitates is added whenever ΔN is higher than a given fraction of the total precipitate density, which we have chosen to be 10^{-8}. This procedure avoids having precipitate size classes that contain too high of a number density. A size class of precipitates is removed when the radius becomes less than 1/10 of the critical radius.

2.2.5. Parameters fit to the model

The key parameters of this model are the interface energy, the diffusion coefficient of yttrium in ferrite, and the solubility product K_S as a function of temperature. K_S is assumed to follow the form:

$$\ln K_{Y_2O_3} = -\frac{A}{T} + B. \tag{10}$$

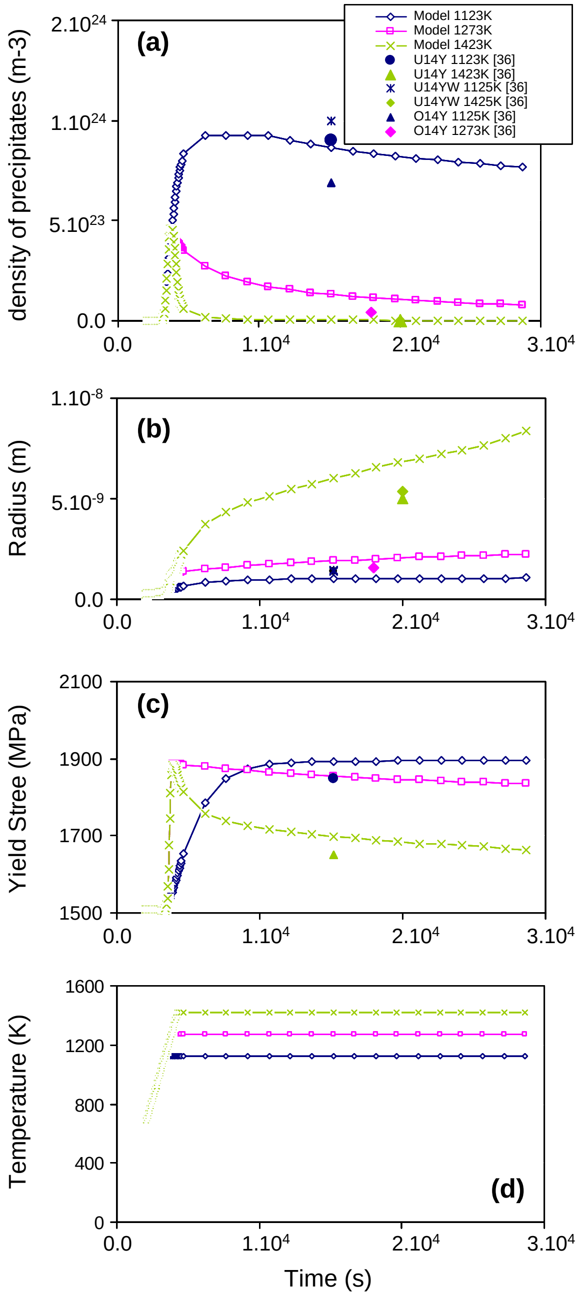

Fig. 1. Comparison between experimental data summarize in Table 1 and the theoretical model of the evolution of the density (a) and size (b) of precipitates, and (c) yield stress as a function of time for the different anisothermal heat treatments given in (d). The alloy compositions are given in Table 1. The temperature varies from 1125 K to 1425 K.

Because there is no experimental data available on these parameters, they have been treated as adjustable parameters within our NGC model to fit the experimental data of Alinger [36]. The resulting model predictions are presented in Fig. 1 and compared to the available data of Alinger [36]. As shown in Fig. 1, a satisfactory agreement has been obtained for a temperature heating rate of 0.33 K/s with a hold temperature of either 1125 or 1275 or 1425 K in an Fe–0.13 at.%Y–0.18 at.%O alloy by choosing:

$$\begin{aligned} A &= 29{,}200\ \text{K} \\ B &= 1.33 \\ \gamma &= 0.4\ \text{J m}^{-2} \\ D_Y^{Fe} &= 1\times10^{-5}\exp\left(-\tfrac{3.25}{kT}\right)\text{m}^2\ \text{s}^{-1} \end{aligned} \tag{11}$$

The interface energy is low but on the same order of magnitude as that found in the literature for incoherent and semi-coherent interfaces (between 0.3 and 2.5 J m^{-2}) [48]. The solubility product is also weak. The decreased solubility product and the low diffusion coefficient have the effect of accelerating the nucleation and the growth stage, and slowing down the coarsening stage of the Y_2O_3 precipitation kinetics.

Since there are few experimental data points, many sets of parameters were tested. All of them required a low solubility limit and a small diffusion coefficient to match the experimental data. Nevertheless, we have three adjustable parameters and five data points, which should be enough to provide a qualitative estimation.

3. Precipitation hardening modeling

The aim of this model is to describe the complete aging sequence during an anisothermal heat treatment and therefore the transition between shearing and by-passing of nanoparticles, which controls the peak strength of the material along with the interparticle spacing. The ultra high density of nanoclusters is the major source of dispersed obstacle hardening. Many other contributions must be included to accurately represent the yield strength. These include: (1) the contribution to strengthening in an unalloyed polycrystalline iron matrix including minor impurities, (2) the intrinsic lattice resistance to dislocation slip, (3) the high dislocation density, and (4) the fine grain size. The details of these different contributions are summarized in this sub-section:

- as estimated in [36], the unalloyed Fe offers a contribution σ_U of 125 MPa at ambient temperature and the contribution σ_I of the impurities in solid solution for a concentration of 15 at.%Cr and 0.8 at.%W contribute 250 MPa;
- the forest hardening contribution to the flow stress is given by:

$$\sigma_{FD} = M\alpha Gb\sqrt{\rho}, \tag{12}$$

where α is a material dependent constant between 0.15 and 0.5 [49], M is the Taylor factor equal to 3.06, G is the shear modulus equal to 80 GPa, b is the Burgers vector (taken to be equal to about 2.5×10^{-10} m) and ρ is the dislocation density. It is ranged from 10^{13} m^{-2} (for fully recrystallized nano-structured ferritic alloys) to 3×10^{15} m^{-2} (for as-milled powders). We took an average value equal to 5×10^{14} m^{-2}.

- the contribution of the grain size is taken to be equal to:

$$\sigma_{GS} = \frac{k_g}{\sqrt{d_g}}, \tag{13}$$

where k_g is the Hall–Petch factor estimated to 0.2 MPa and d_g is the grain size. Depending on the anisothermal heat treatment history, it is ranged from 0.5×10^{-6} to 50×10^{-6} m. We took an average value equal to 1×10^{-7} m.

- the contribution of the dispersed obstacles depends on the dislocation interaction and bypass mechanism. When oxide precipitates are coherent with the ferritic matrix and the applied strain is sufficient [50], precipitates are sheared by dislocations. Otherwise, the mechanisms are likely much more complex. According to Refs. [40–42], the line tension of the dislocation around an oxide nanoparticle is totally or partially relaxed. The dislocation is pinned and a constraint is required for dislocation motion. When the limiting mechanism is the climb of the dislocation, the critical constraint is proportional to the Orowan stress. It depends on both the interparticle distance λ and the size of the particle r. Note that if the interparticle distance 2λ is much higher than the radius r of the oxide particles, the Orowan stress only depends on $1/\lambda$. When the limiting mechanism is the detachment of the dislocation, the critical constraint is inversely proportional to λ and does not depend on the size of the particle. Thus, the yield stress seems strongly to depend on the interparticle distance as well as the radius of the particle. Transmission Electronic Microscopic studies [51] seem to support these conclusions.

The model used in this study for the contribution from the precipitates to the yield stress is derived from Orowan hardening models, based on the bypass mechanism for hard obstacles [40–42]. This has been treated in detail previously; see Ref. [36]. The contribution from the precipitates to the flow stress can be expressed as:

$$\sigma_P = 0.8MT_{trans}(r)\frac{Gb}{Sp}, \tag{14}$$

where Sp is the particle spacing in the glide plane depending on the average size r of the obstacles and the volume fraction f_v:

$$Sp \approx \frac{1.18r}{\sqrt{f_v}} - 0.81r. \tag{15}$$

Finally, $T_{trans}(r)$ is the strength factor that may depends on the obstacle size. It has been fitted to experimental yield stress measurements by Alinger [36] and is given by:

$$T_{trans}(r) = -0.017 + 0.374\ln\left(\frac{r}{2b}\right). \tag{16}$$

Full details of the fit can be found in Chapter 6 (Section 6.5) in Ref. [36]. This strength scaling is the same as for the $\frac{\ln(\frac{r}{b})}{2\pi}$ term in Orowan hardening models, based on the bypass mechanism for hard obstacles, and is rationalized from attractive dipole interactions between highly bowed dislocation segments. Taking $b = 2.5 \times 10^{-10}$ m, we have two different cases; if $r < 5 \times 10^{-10} \exp(0.0026738(17 + 1000\,T_{\text{trans}}))$, then the precipitates are sheared by the dislocation, otherwise the dislocation bypass the precipitates by Orowan looping.

Finally, the contributions of the yield stress σ_y are assumed to sum linearly, and thus, the yield strength can be expressed as:

$$\sigma_y = \sigma_u + \sigma_i + \sigma_{FD} + \sigma_{GS} + \sigma_P. \tag{17}$$

4. Numerical model results

This section is devoted to understanding the precipitation kinetics for alternate time–temperature histories associated with either anisothermal or isothermal heat treatment, using the set of parameters fit to the experimental data of Alinger [36]. All the anisothermal heat treatments start at 600 K. Bellow this temperature, the diffusion coefficients of the different species are too small to observe an influence on the precipitation kinetics.

Results for different anisothermal heat treatments will first be analyzed, and then the role of the anisothermal versus isothermal heat treatments on the density and size of the precipitates will be discussed. A final section will discuss the effect of different yttrium and oxygen supersaturations on the Y_2O_3 precipitation kinetics. In each case, the yield stress will be determined and analyzed as a function of precipitate density and size.

4.1. Density of precipitates and average radius: comparison between SANS experimental data and numerical model

Anisothermal heat treatments were performed with a temperature ramp of 0.33 K/s up to 1125 K (case 1), 1273 K (case 2) and 1425 K (case 3) for an Fe–0.13 at.%Y–0.18 at.%O alloy. The modeling results are presented in Fig. 1, in which the precipitate number density, average radius, and yield stress are shown as a function of time, along with the temperature history for each case.

In Fig. 1a, corresponding to case 1, the density of precipitates increases during the ramp rise up to the temperature plateau at 1125 K, where it continues to increase to a density approaching 1×10^{24} m^{-3}. The average precipitate radius (Fig. 1b) and the yield stress (Fig. 1c) also increase during the temperature ramp. Then, the precipitate density slowly decreases (8×10^{23} m^{-3}). This is consistent with a transition of the precipitation kinetics to the growth and coarsening stage. The average radius is about 1 nm, as shown in Fig. 1b. However, the coarsening stage evolves very slowly. It seems to be frustrated due to the weak solubility product and the small diffusion coefficient. Since both precipitate size and density evolve very slowly, the interparticle spacing evolves similarly. This means that the yield stress exhibits a plateau. The peak resulting from the shearing to Orowan looping bypass transition is not observed in this case.

For the second and the third heat treatment cases, which have higher temperature plateaus, the modeling predictions of the precipitation kinetics are indeed different. The precipitate number density increases only during the initial part of the temperature ramp (up to 1150 K) and then begins to decrease more rapidly during the anisothermal heat treatment. The yield stress exhibits the same behavior, namely that the strength increases only during the first part of the temperature ramp. Since the driving force for precipitation is a function of temperature, the higher temperature lowers the driving force. Moreover, with increasing temperature, both oxygen and yttrium have higher diffusion coefficients in the ferrite. Both favor a lower density of precipitates as a result of a more rapid transition to coarsening mediated growth (Fig. 1a) with increasing consolidation temperature. The coarsening stage evolves faster in both cases 2 and 3 than in case 1. The interparticle spacing of the oxide particles increase as the coarsening stage evolves. In both cases, a transition from dislocation bypass by shearing to one of Orowan looping is predicted. In the third case, the transition is more pronounced than in the second case.

After 25,000 s (∼7 h) of heat treatment, the average precipitate radius in case 2 is twice that in case 1, and the number density of precipitates is around four times lower. For the heat treatment of case 3, the system has clearly reached the coarsening stage after 25,000 s. The precipitate number density is approximately 400 times less than compared to case 1, while the average radius is eight times larger in case 3 than in case 1. The difference in the yield strength between cases 1 and 3 is about 1.2. However, this difference in ratio is only observed at longer times. For the short-time, the yield stress predicted for cases 2 and 3 are of the same order of magnitude as the yield stress of case 1. Thus, many anisothermal heat treatments can give the same yield stress: they depend on the kinetic paths of precipitation. Note that the predicted yield strengths are in the range between 1500 and 2000 MPa. These values are very consistent with the experimental data of Alinger [36], notably for the U14Y alloys where yield stresses have been experimentally determined, although there are a large number of assumptions inherent in the strength prediction.

4.2. Effect of temperature heating rate on precipitation kinetics

Model calculations were performed to investigate the effect of heating rate on the Y_2O_3 precipitation kinetics. Heating rates equal to 0.25 K/s, 0.33 K/s and 0.41 K/s have been modeled up to 1125 K (Fig. 2) or 1425 K (Fig. 3), and compared with an isothermal heat treatment at 1125 K (Fig. 2) or 1425 K (Fig. 3) for the Fe–0.13 at.%Y–0.18 at.%O alloy. Again, the precipitate number density and average radius, and the yield stress are plotted as a function of time.

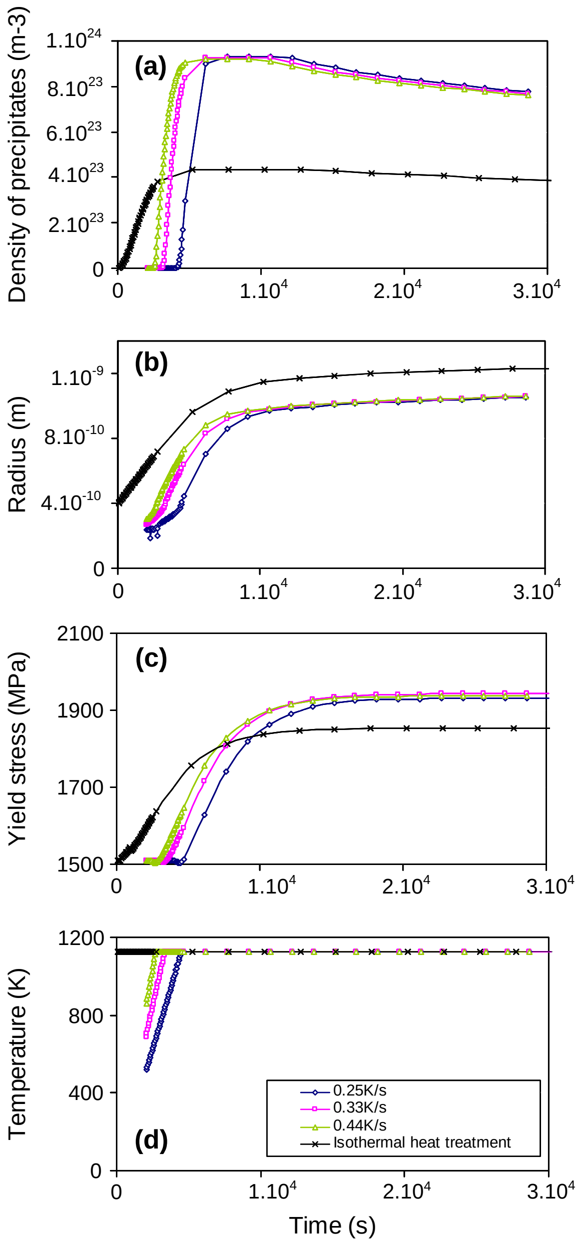

Fig. 2. Evolution of the density (a) and the size (b) of precipitates, and (c) the yield stress as a function of time during different anisothermal heat treatment depending on the speed of the temperature ramp (d). The alloy composition is Fe–0.13 at.%Y–0.18 at.%O and the temperature is 1125 K.

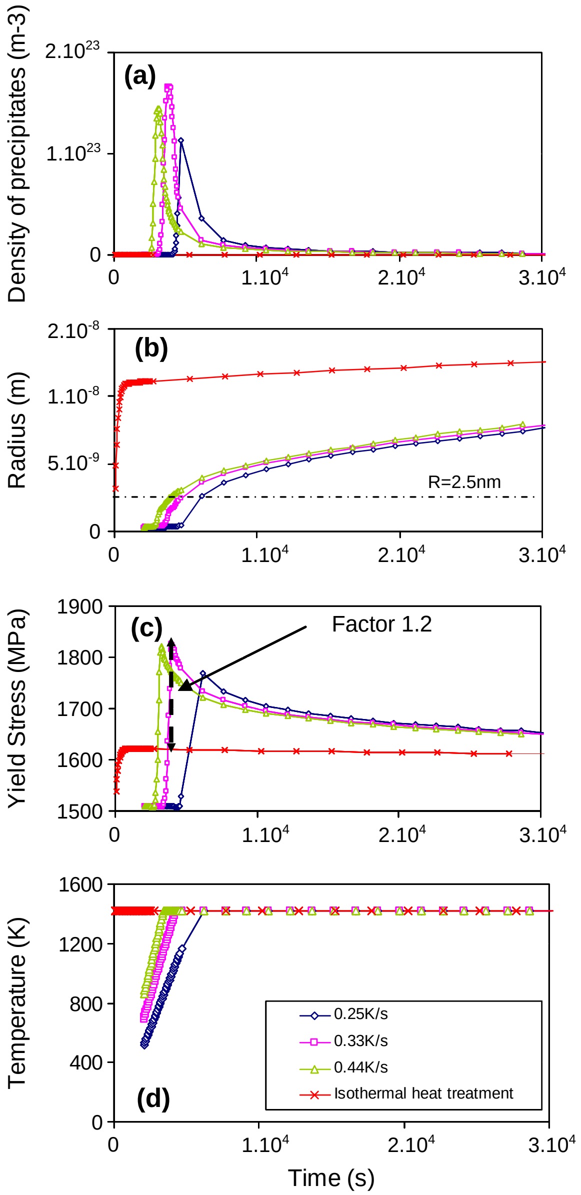

Fig. 3. Evolution of the density (a) and the size (b) of precipitates, and (c) the yield stress as a function of time during different anisothermal heat treatments and different temperature ramp speeds (d). The alloy composition is Fe–0.13 at.%Y–0.18 at.%O and the temperature is 1425 K.

In Fig. 2a, it is clear that the precipitate density increases with higher heating rates. However, this effect appears short-lived, since after 750 s, all the precipitate densities are approximately the same regardless of the temperature ramp; the average radii and the yield stress show similar behavior (Fig. 2b and c). As explained in the previous section, the peak resulting from the shearing to Orowan looping transition is not predicted to occur for the anisothermal heat treatment with a plateau at 1125 K.

Comparing the anisothermal to the isothermal heat treatment, the precipitate density initially increases much more rapidly for the isothermal heat treatment at 1125 K, but after 750 s the density remains lower and the difference between the four cases is not so significant. Similar behavior is also observed for the average radius and the yield stress. Thus, it is concluded that even if the initial time evolutions of the precipitate kinetics are different, the effect of heating rate is negligible for longer aging times at 1125 K, although the isothermal heat treatment at 1125 K produces slightly larger, slightly less numerous precipitates.

Fig. 3a shows a similar comparison to investigate the effect of heating rate for a plateau of temperature at 1425 K. As in the previous lower temperature case, the precipitate density initially increases faster with increasing heating rate. However, multiple peaks describing the maximum of precipitate densities appear (Fig. 3a), which are also observed in the prediction of the maximum yield stress (Fig. 3c). The maximum of the precipitate density correspondent to the maximum of the yield stress with the condition that precipitate should have an average radius equal to 2.5 nm (see line in Fig. 3b). Then, the precipitate densities decrease, while the average radii increase. The coarsening stage of the Y_2O_3 precipitates is observed to occur since the plateau temperature is much higher than in the previous case, and hence the Y atoms diffuse more rapidly. Since the precipitate density decreases, the interparticle spacing increases. The yield stress then decreases during the coarsening stage, and correspondingly the model predicts that a shearing to Orowan looping transition occurs. After 800 s, both the density and radius of the Y_2O_3 precipitates, and the yield stress are of the same order of magnitude, independent of the anisothermal heat treatment.

Concerning the isothermal heat treatment case at 1425 K, the density of precipitates is always smaller than during an anisothermal heat treatment, which is quite different to the case at 1125 K. For example, after 1000 s, the average radius of precipitates obtained during an isothermal heat treatment is about twice that of the anisothermal heat treatment, while the density of precipitates is about 1000 times smaller and the yield stress is 12% lower. During an isothermal heat treatment, the driving force for precipitation is always lower than during an anisothermal heat treatment. In addition, at the beginning of the thermal heat treatment, the diffusion coefficient is faster during an isothermal heat treatment than during an anisothermal heat treatment. This means that a quick nucleation stage is more rapidly followed by the growth stage. Fig. 3b shows that the precipitate average radius increases rapidly at short time. After 25,000 s, the precipitate number density is about 100 times that of the anisothermal heat treatment, and the average radius is twice as large. However, these significant differences at the end of the heat treatment have only a moderate effect on the predicted yield stress, which is only 5% lower. This is ascribed to the fact that the coarsening decreases the precipitate density and thereby increases the interparticle spacing, but increases the precipitate size and thereby the obstacle strength due to the transition in bypass mechanism.

Thus it has been demonstrated that anisothermal heat treatments, by favoring the higher number of smaller precipitates compared to an isothermal heat treatment (especially as the thermodynamic driving force is decreased), can strongly influence the size and number distribution of the precipitates and correspondingly, increase the yield stress up to a factor 1.2 (Fig. 3c).

4.3. Effect of Y and O supersaturation on the precipitation kinetics

The model was also used to simulate anisothermal heat treatments for different of Y and O supersaturations with a heating rate of 0.25 K/s to a plateau of 1125 K. The precipitate number density and average radius are plotted in Fig. 4 as a function of time. For the sake of brevity, only the yttrium concentrations are provided in the caption, whereas the corresponding oxygen concentration is obtained by multiplying the yttrium concentration by 1.5.

Fig. 4a and b shows that for a yttrium concentration between 0.1 and 0.3 at.%, and corresponding oxygen concentration between 0.15 and 0.45 at.%, the effect of higher concentration is to increase the precipitate number density and lower the average radius, thereby enhancing the nucleation rates, as expected.

The yield stress, which depends on the density and precipitate size, begins to increase as the precipitate number density increases with a precipitate radius larger than 0.5 nm (Fig. 4c). As in the previous simulations with a temperature plateau of 1125 K, the precipitate size remained below the threshold for a transition between the shearing and Orowan looping mechanism, independent of the Y and O super saturations investigated here. Again, it is believed that the weak solubility product and the low diffusion coefficient have a similar effect, namely to accelerate the nucleation and early growth stages, but to slow down the subsequent coarsening of the precipitate distribution.

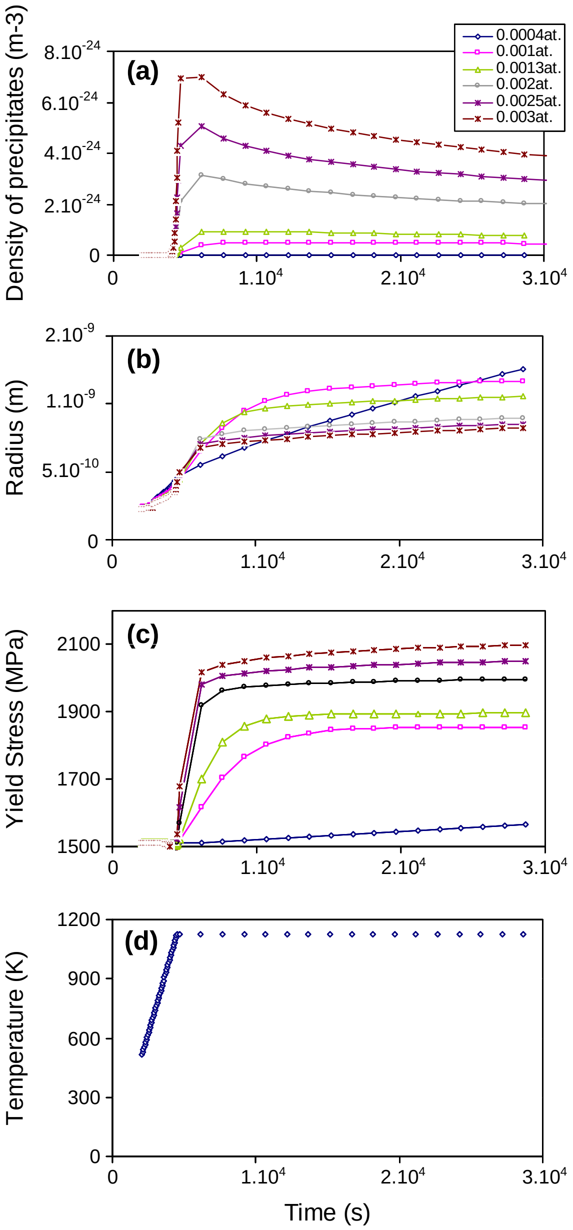

Fig. 4. Evolution of the density (a) and the size (b) of precipitates, and (c) the yield stress as a function of time for different cases of supersaturation during an anisothermal heat treatment where temperature is ramped at 0.25 K/min to 1125 K (d). For the sake of conciseness, only the yttrium concentrations are written in the caption. The corresponding oxygen concentration is given by multiplying the yttrium concentration by about 1.5.

For the lowest concentration of 0.04 at.%Y and 0.06 at.%O, the results are completely different. The precipitate density remains lower than at higher super saturations for all times during the anisothermal heat treatment. Yet, Fig. 4b shows that the precipitate size increases more slowly than for higher supersaturations.

This can be explained by the fact that the nucleation–growth stages are reached more rapidly at higher supersaturations, while the system is still in a nucleation stage at lower concentrations. The largest precipitate number density occurs between the highest and the lowest concentration limits simulated here. After 25,000 s, the precipitates are about 450 times more numerous for the highest concentration of 0.3 at.%Y, as compared to the lower concentration of 0.04 at.%Y. As well, the average radius is about 1.5 times smaller, and the yield stress is 35% higher with the higher level of super saturation.

Similar behavior is observed for the different cases of anisothermal heat treatments. We can thus conclude that finer precipitate size distributions are obtained for cases of higher supersaturations within the range of heat temperature treatments studied here. The finer precipitate size distribution also produces the largest strength increases.

5. Conclusion

The precipitation kinetics of Y_2O_3 in ferrite has been studied using a classical precipitate nucleation–growth–coarsening model, adapted to treat anisothermal heat treatment conditions as well as to predict the strength using a dispersed barrier hardening model. The key parameters within the model are the solubility product of Y_2O_3 in ferrite and the diffusion coefficient of yttrium atoms in ferrite, which are very difficult to determine from either experiments or first principles calculations. Thus, these parameters have been estimated by fitting the model predictions to experimental small angle neutron scattering results of Y_2O_3 precipitate size distributions in a mechanically alloyed and consolidated Fe–15 at.%Cr–0.13 at.%Y–0.18 at.%O ferritic alloy. The structural hardening model incorporates both the precipitate size and number density to predict the yield strength, and includes a size dependent strength parameter that involves a transition from precipitate shearing at small size to Orowan looping for larger precipitates.

It has been demonstrated that anisothermal heat treatment, by favoring the higher number of smaller precipitates compared to an isothermal heat treatment, increases the yield stress. We conclude that, to obtain the highest density of fine precipitates and consequently the highest yield stress, an anisothermal heat treatment with a low temperature plateau (e.g. 1125 K) and a high supersaturation of Y and O are preferred. In this case, the yield strength can be multiply by a factor 1.35 compared to the precipitate distribution when the alloy composition has a lower concentration of Y and Ti during an isothermal heat treatment. Thus, it is important to carefully optimize both the heat treatment and the alloy composition in order to better control the kinetic path of precipitation and correspondingly, the resulting mechanical strength.

Acknowledgements

We gratefully acknowledge useful and stimulating discussions with Yves Bréchet. The authors gratefully acknowledge the financial support of the National Science Foundation under Contract NSF DMR 0548259 and the Department of Energy, Office of Fusion Energy Sciences under Grant DE-FG02-04GR54750.

References

[1] S. Ukai, M. Fujiwara, J. Nucl. Mater. 307–311 (2002) 749.
[2] R. Lindau, A. Moeslang, M. Schirra, P. Schlossmacher, M. Klimenkov, J. Nucl. Mater. 307–311 (2002) 769.
[3] J. Bertsch, R. Lindau, A. Moeslang, J. Nucl. Mater. 233–237 (1996) 276.
[4] G.R. Odette, G.E. Lucas, J. Nucl. Mater. 179 (1991) 572.
[5] N. Miyaji, Y. Abe, S. Ukai, S. Onose, J. Nucl. Mater. 272 (1999) 173.
[6] G.R. Odette, M.J. Alinger, B.D. Wirth, Annu. Rev. Mater. Res. 38 (2008) 471.
[7] M.K. Miller, K.F. Russell, D.T. Hoelzer, J. Nucl. Mater. 351 (2006) 261.
[8] M.A. Sokolov, D.T. Hoelzer, R.E. Stoller, D.A. McClintock, J. Nucl. Mater. 367–370 (2007) 213.
[9] D.A. McClintock, M.A. Sokolov, D.T. Hoelzer, R.K. Nanstad, J. Nucl. Mater. 392 (2009) 353.
[10] D.A. McClintock, M.A. Sokolov, D.T. Hoelzer, R.K. Nanstad, J. Nucl. Mater. 386 (2009) 307.
[11] M.J. Alinger, G.R. Odette, D.T. Hoelzer, Acta Mater. 57 (2009) 392.
[12] D.T. Hoelzer, J. Bentley, M.A. Sokolov, M.K. Miller, G.R. Odette, M.J. Alinger, J. Nucl. Mater. 367 (2007) 166.
[13] T. Yamamoto, G.R. Odette, P. Miao, D.T. Hoelzer, J. Bentley, N. Hashimoto, H. Tanigawa, R.J. Kurtz, J. Nucl. Mater. 367 (2007) 399.
[14] P. Pareige, M.K. Miller, R.E. Stoller, D.T. Hoelzer, E. Cadel, B. Radiguet, J. Nucl. Mater. 360 (2007) 136.
[15] R.L. Klueh, J.P. Shingledecker, R.W. Swindeman, D.T. Hoelzer, J. Nucl. Mater. 341 (2005) 103.
[16] M.K. Miller, K.F. Russell, E.A. Kenik, D.T. Hoelzer, J. Nucl. Mater. 13 (2005) 387.
[17] N.Y. Iwata, R. Kasada, A. Kimura, T. Okuda, M. Inoue, F. Abe, S. Ukai, S. Ohnuki, T. Fujisawa, ISIJ Int. 49 (2009) (1914).
[18] T. Kaito, S. Ukai, A.V. Povstyanko, V.N. Efimov, J. Nucl. Sci. Technol. 46 (2009) 529.
[19] S. Ukai, S. Ohtsuka, T. Kaito, H. Sakasegawa, N. Chikata, S. Hayashi, S. Ohnuki, Mater. Sci. Eng. A – Struct. Mater. Prop. Microstruct. Process. 510–511 (2009) 115.
[20] T. Kaito, S. Ohtsuka, M. Inoue, T. Asayama, T. Uwaba, S. Mizuta, S. Ukai, T. Furukawa, C. Ito, E. Kagota, R. Kitamura, T. Aoyama, T. Inoue, J. Nucl. Mater. 386 (2009) 294.
[21] S. Ohtsuka, T. Kaito, M. Inoue, T. Asayama, S.W. Kim, S. Ukai, T. Narita, H. Sakasegawa, J. Nucl. Mater. 386 (2009) 479.
[22] A. Kimura, R. Kasada, A. Kohyama, H. Tanigawa, T. Hirose, K. Shiba, S. Jitsukawa, S. Ohtsuka, S. Ukai, M.A. Sokolov, R.L. Klueh, T. Yamamoto, G.R. Odette, J. Nucl. Mater. 367 (2007) 60.
[23] J.S. Langer, A.J. Schwartz, Phys. Rev. A21 (1980) 948.
[24] R. Kampmann, R. Wagner, in: Decomposition of Alloys: The Early Stage, Pergammon Press, Oxford, 1984, p. 91.
[25] D. Gendt, Ph.D. Thesis, Université de Paris XI, Orsay, France, 2001.
[26] P. Maugis, M. Gounet, Acta Mater. 53 (2005) 3359.
[27] H.R. Shercliff, M.F. Ashby, Acta Mater. 38 (1990) 1789.
[28] A. Deschamps, Y. Bréchet, Acta Mater. 47 (1998) 293.
[29] F. Perrard, A. Deschamps, P. Maugis, Acta Mater. 55 (2007) 1255.
[30] H.R. Shercliff, M.F. Ashby, Acta Mater. 38 (1990) 1803.
[31] O.R. Myhr, O. Grong, Acta Mater. 48 (2000) 1605.
[32] O.R. Myhr, O. Grong, S.J. Anderson, Acta Mater. 75 (2001) 65.
[33] O.R. Myhr, O. Grong, H.G. Fjaer, C.D. Marioara, Acta Mater. 52 (2004) 4997.
[34] A. Simar, Y. Bréchet, B. De Meester, A. Denquin, T. Pardoen, Acta Mater. 55 (2007) 6133.
[35] N. Kamp, A. Sullivan, R. Tomasi, J. Robson, Acta Mater. 54 (2006) 2003.
[36] M. Alinger, Ph.D. Thesis, University of Santa Barbara, USA, 2004.
[37] V. Gerold, Dislocation in Solids, vol. 4, North Holland, Amsterdam, 1979.
[38] A.J. Ardell, Metall. Trans. A16 (1985) 2131.
[39] B. Reppich, Materials Science and Technology, a Comprehensive Treatment, vol. 6, VCH, Weinheim, 1993.
[40] D.J. Srolovitz, M.J. Luton, R.A. Petrovik-Luton, D.M. Barnett, W.D. Nix, Acta Metall. 132 (7) (1984) 1079.
[41] E. Arzt, D.S. Wilkinson, Acta Metall. 34 (10) (1986) 1893.
[42] J. Rosler, E. Arzt, Acta Metall. 36 (4) (1988) 1043.
[43] I. Monnet, Ph.D. Thesis, Ecole Centrale de Paris, France, 1999.
[44] M.J. Alinger, G.R. Odette, D.T. Hoelzer, J. Nucl. Mater. 329–333 (2004) 382.
[45] J. Gibbs, The Scientific Papers, vol. 1, Dover, N.Y., 1961.
[46] A. Perini, G. Jacucci, G. Martin, Phys. Rev. B 29 (1984) 2689.
[47] J. Christian, The Theory of Transformation in Alloys and Metals, Pergamon Press, Oxford, 1975.
[48] J.M. Howe, Interfaces in Materials, Wiley-Interscience, 1997.
[49] M.F. Ashby, in: A. Kelly, R.B. Nicholson (Eds.), Strengthening Methods in Crystals, Elsevier, Amsterdam, 1971.
[50] Y. Bréchet, F. Louchet, Acta Mater. 37 (1989) 2469.
[51] V.L. Nardone, D.E. Matejczyk, J.K. Tien, Acta Metall. 32 (9) (1984) 1509.